Microfluidics and Nanofluidics (2019) 23:22
https://doi.org/10.1007/s10404-018-2182-x

RESEARCH PAPER

# Suspension of deformable particles in Newtonian and viscoelastic fluids in a microchannel

**Amir Hossein Raffiee[1] · Sadegh Dabiri[1,2] · Arezoo M. Ardekani[1]**

Received: 16 October 2018 / Accepted: 26 December 2018 / Published online: 17 January 2019


**Abstract**
In this paper, we study a suspension of cells at a moderate volume fraction flowing in a microchannel filled with Newtonian or viscoelastic fluids and investigate the role of cell size, cell volume fraction, inertia, deformability, and fluid elasticity on the cell distribution. Our results suggest that the use of constant-viscosity viscoelastic fluid pushes the cells toward the channel centerline which can be used in microfluidic devices used for cell focusing such as cytometers. The cell-free layer increases which provides larger gap for separating rare cells in microfluidic devices. Furthermore, we show that the volumetric flow rate can be significantly enhanced with the addition of polymers in the suspending fluid. This effect enhances the processing speed which is of interest in designing microfluidic devices. This fundamental study can provide insight on the role of rheological properties of the fluid that can be tuned to control the motion of the cells for efficient design of microfluidic devices.

**Keywords** Cell migration in polymeric fluids · Cell focusing · Elasto-inertial cell migration

## 1 Introduction

The motion of synthetic capsules and living cells in microchannels has been the subject of numerous studies in the last decade due to its significance in engineering and biomedical applications (Popel and Johnson 2005; Pozrikidis 2003; Cooley et al. 2018). Cell sorting and separation are common processes that are used for various purposes such as separation of leukocytes from blood used in DNA sequencing (Gossett et al. 2010). Early diagnosis of lethal diseases such as cancer (van de Stolpe et al. 2011) can be conducted by isolation of rare cells in blood, which is a complex suspension of cells. Furthermore, fractionated healthy blood components are used for different therapeutic applications such as platelet transfusion (Sethu et al. 2006). Cell isolation and enrichment provide a better platform to biologists to study and analyze various properties of living cells (Karimi et al. 2013; Gossett et al. 2010). In this regard, microfluidic devices provide a platform to achieve aforementioned needs while overcoming challenges such as sample contamination, cost, and complexity of the procedures (Paiè et al. 2017). Besides, these devices offer higher accuracy for analysis and increased automation of the process (Chung and Kim 2007; Godin et al. 2008). Accordingly, there is a high demand for developing techniques to precisely control trajectories of cells and manipulate them in a desired manner. Some of the proposed techniques employ external factors such as electric (Pethig 2010), magnetic (Pamme 2006), and acoustic (Friend and Yeo 2011) fields and sheath flows (Sundararajan et al. 2004; Lancaster et al. 2005; Howell Jr et al. 2008). Even though they can offer high-throughput sample processing, the complexity of the procedure and high-cost limits their utilization in clinical applications (Gossett et al. 2010). Furthermore, these methods require cell manipulation that may change biological properties of the cells (Del Giudice et al. 2017). Hence, there is a growing interest in employing label-free techniques that take advantage of physical properties of the cells such as size, shape, and deformability to control their trajectories in microfluidic devices (Paiè et al. 2017; Del Giudice et al. 2017; Gossett et al. 2010). Inertial microfluidics are among the proposed techniques that use inertial forces to induce cell migration in microchannels (Di Carlo et al. 2007,

This article is part of the topical collection "Particle motion in non-Newtonian microfluidics" guest edited by Xiangchun Xuan and Gaetano D'Avino.

✉ Arezoo M. Ardekani
ardekani@purdue.edu

[1] School of Mechanical Engineering, Purdue University, West Lafayette, IN 47907, USA

[2] Department of Agricultural and Biological Engineering, Purdue University, West Lafayette, IN 47907, USA

2009; Choi et al. 2011). In this technique, cells focus at an equilibrium position depending on their physical properties (Hur et al. 2010; Kunze et al. 2015; Di Carlo 2009). The particles flowing in a Newtonian fluid follow the streamlines without any transversal migration for low Reynolds numbers (Ho and Leal 1974). With increasing the Reynolds number, the inertial force becomes important and the cross-streamline migration of particles is observed (Leshansky et al. 2007; Lee et al. 2013). In this case, the particle experiences two opposing forces: (1) shear-gradient induced force that pushes the particle toward the wall (Asmolov 1999) and (2) the wall-induced repulsive force that drives it toward the channel center (Zeng et al. 2005). The balance between these two forces determines the equilibrium position of the flowing particle in the channel cross section (Li et al. 2015). This phenomenon was first observed by Segre (1961). In their experiments, randomly distributed particles at tube inlet assembled at an annulus with radius of 0.6 times the radius of the tube. This result was later confirmed numerically (Feng et al. 1994), analytically (Schonberg and Hinch 1989), and experimentally (Karnis et al. 1966). Previous investigations show that the deformability of the cell can affect its trajectory in the microchannel (Raffiee et al. 2017b; Schaaf and Stark 2017; Kilimnik et al. 2011; Saadat et al. 2018). Due to deformability of cell membrane, a deformability-induced force is generated and the interplay of all the above forces governs the equilibrium position of the flowing cells (Raffiee et al. 2017b). In our previous work (Raffiee et al. 2017b), we studied the effect of cell deformability on the equilibrium position of a single deformable cell. Our results show that deformability-induced force drives the cells toward the channel centerline in a Newtonian fluid. Recent studies on microfluidic devices introduced an alternative way for cell focusing by adding a polymer to the suspending fluid (Lu et al. 2017; D'Avino et al. 2017; Faridi et al. 2017). In this method, the polymer chains in the fluid are stretched and generate an uneven normal stress on the flowing particles. This phenomenon leads to a net elastic force that interacts with the inertial force and affects the migration dynamics and equilibrium position of the particle (Del Giudice et al. 2015, 2017). This phenomenon has been experimentally and analytically (Leshansky et al. 2007; Yang et al. 2011; D'Avino et al. 2012; Li et al. 2015) observed. The particle migration depends on the fluid rheology, cell size, channel geometry, and volumetric flow rate (Villone et al. 2013; Li et al. 2015). There are several experimental studies that showed promising results for cell separation and focusing using polymeric fluid as the suspending fluid. Lim et al. (2014) used hyaluronic acid (HA) in the suspending fluid and successfully focused solid particles and leukocytes at the channel center. Furthermore, the same method was used to separate human breast carcinoma and leukocyte cells in a straight microchannel (Nam et al. 2015) which highlights the effect of cell size and deformability on the particle migration flowing in a viscoelastic polymeric fluid. The effect of size and deformability was also observed Liu et al. (2015), where solid particles, living cells, and bacteria were separated by focusing in different locations in the channel cross section. Previous studies (Seo et al. 2014; Leshansky et al. 2007; Romeo et al. 2013; Raffiee et al. 2017b) show that fluid rheological properties are important on the dynamics of cell migration in microchannels. In our previous work (Raffiee et al. 2017b), we have shown that the focusing position of the cell in a constant-viscosity fluid is closer to the centerline compared to that in a Newtonian fluid. However, the shear-thinning properties of a Geisekus fluid can significantly modify the equilibrium position. The equilibrium position of cell also depends on the cell size, deformability, and volumetric flow rate.

Despite the importance of the dynamics of cell suspensions in a microchannel, the previous experimental and computational studies focus on the migration of cells in a dilute regime. This limitation prevents us to evaluate the performance of the developed techniques for rich samples such as blood which has higher cell concentrations. The optical techniques cannot be effectively used for quantification of samples at high cell concentrations. To overcome this limitation, we focus on a suspension of deformable cells in Newtonian and polymeric fluids in semidilute and concentrated regimes and investigate the role of various factors including cell size, deformability, inertia, and viscoelasticity of the suspending fluid. Our results provide fundamental understanding of the dynamics of suspension of cells in a straight microchannel used in various microfluidic devices.

## 2 Methodology

### 2.1 Governing equations

Dynamics of the deformable cells flowing in a microchannel is governed by the momentum and continuity equations. In this study, we assume that the inner fluid of the cell and suspending fluid is incompressible. Therefore, we have

$$\nabla.\mathbf{u} = 0, \tag{1}$$

$$\frac{\partial(\rho\mathbf{u})}{\partial t} + \nabla.(\rho\mathbf{u}\mathbf{u}) = -\nabla p + \nabla.\boldsymbol{\tau} + \mathbf{F}. \tag{2}$$

Here, $\rho$ is the density of the fluid, $t$ denotes the time, $\mathbf{u}$ is the velocity vector, and $p$ and $\boldsymbol{\tau}$ represent pressure and stress tensor, respectively. The stress tensor in a Newtonian fluid is a function of fluid viscosity $\mu$ and strain rate tensor $\mathbf{D} = \nabla\mathbf{u} + \nabla\mathbf{u}^{\mathrm{T}}$, where $\boldsymbol{\tau} = \mu\mathbf{D}$. We use a front-tracking (Unverdi and Tryggvason 1992) method to track the interface and capture the change in fluid properties across the membrane. In this method, a single set of equations is solved in the entire computational domain. In Eq. (2), $\mathbf{F}$ represents

the smoothed elastic force generated due to the deformation of cell membrane which can be obtained as

$$\mathbf{F}(\mathbf{x},t) = \int_{\partial B} \boldsymbol{f}(\mathbf{x}_i,t)\delta(\mathbf{x}-\mathbf{x}_i)\mathrm{d}V. \tag{3}$$

Here, $\boldsymbol{f}$ is the membrane resistive force exerted on the fluid. This force is zero everywhere in the domain except for the membrane interface. In Eq. (3), $\mathbf{x}$ and $\mathbf{x}_i$ denote an arbitrary point in the computational domain and a point on the cell membrane, respectively. Furthermore, $\delta$ and $V$ are the Dirac delta function and volume, respectively. To distribute the resistive force on Eulerian grid points surrounding the membrane, a smoothed delta function is employed:

$$\delta(\mathbf{x}) = \tilde{D}(x)\tilde{D}(y)\tilde{D}(z), \tag{4}$$

$$\tilde{D}(x) = \frac{1}{4\Delta}\left(1+\cos\left(\frac{\pi}{2\Delta}x\right)\right), |x| \le 2\Delta, \tag{5}$$

where $\Delta$ is the Eulerian grid size. To simulate the cell membrane, we use the Skalak et al. (1973) model. Ramanujan and Pozrikidis (1998) showed that the Skalak model can capture the behavior of deformable cells under various conditions and their results agreed well with experiments (Chang and Olbricht 1993). In this model, the cell is assumed to behave as a deformable capsule that has a resistance against shear deformation and area dilatation. Accordingly, a strain energy function is assigned to the membrane as follows:

$$W = \frac{E_\mathrm{s}}{12}((\epsilon_1^2+\epsilon_2^2-2)^2+2(\epsilon_1^2+\epsilon_2^2-2)-2(\epsilon_1^2\epsilon_2^2-1)) + \frac{E_\mathrm{a}}{12}(\epsilon_1^2\epsilon_2^2-1)^2, \tag{6}$$

where $E_\mathrm{s}$ and $E_\mathrm{a}$ denote shear and dilatation moduli and $\epsilon_1$ and $\epsilon_2$ are principal strains. In this study, we consider $\frac{E_\mathrm{a}}{E_\mathrm{s}} = 2$ following Krüger et al. (2014). For the range of Reynolds and Laplace numbers used in this study, the area extension is less than 8%. We use a finite-element method (Charrier et al. 1989) to obtain the force $\mathbf{f}$ in Eq. (3). The validation of this model against previously published results is presented in our previous work (Raffiee et al. 2017a). The Navier–Stokes equations are solved using a finite-volume method. The time derivatives are discretized using an explicit Euler scheme and discretization for the convective and diffusive terms is conducted using Quadratic Upstream Interpolation for Convective Kinematics (Leonard 1979) (QUICK) and central difference schemes, respectively. The pressure–velocity coupling is conducted using a projection method (Chorin 1968).

To solve for a viscoelastic suspending fluid, the total stress $\boldsymbol{\tau}$ is split into two parts: (1) solvent stress tensor $\boldsymbol{\tau}_s$ and (2) polymeric stress tensor $\boldsymbol{\tau}_p$ as follows:

$$\boldsymbol{\tau} = \boldsymbol{\tau}_s + \boldsymbol{\tau}_p. \tag{7}$$

Here, $\boldsymbol{\tau}_s$ can be written as

$$\boldsymbol{\tau}_s = \mu_\mathrm{s}\mathbf{D}, \tag{8}$$

where $\mu_\mathrm{s}$ is the solvent viscosity. In this study, the Oldroyd-B constitutive equation is used to represent the stress tensor:

$$\lambda \overset{\triangledown}{\boldsymbol{\tau}}_p + \boldsymbol{\tau}_\mathbf{p} = \mu_p\mathbf{D}, \tag{9}$$

In this equation, $\mu_p$ is the polymer viscosity and $\lambda$ represents the fluid relaxation time. Equation (9) models a constant-viscosity viscoelastic fluid. Here, $\overset{\triangledown}{\boldsymbol{\tau}}_p$ is the upper convected time derivative defined as

$$\overset{\triangledown}{\boldsymbol{\tau}}_p = \frac{\partial \boldsymbol{\tau}_p}{\partial t} + \mathbf{u}.\nabla\boldsymbol{\tau}_p - \nabla\mathbf{u}\boldsymbol{\tau}_p - \boldsymbol{\tau}_p\nabla\mathbf{u}^\mathrm{T}. \tag{10}$$

The details of the numerical scheme used to solve Eq. (9) and its validation are explained in our previous work (Raffiee et al. 2017a).

## 2.2 Problem setup

In this work, the computational domain is a straight squared channel, as illustrated in Fig. 1. The edge of the channel is $2W$ and the channel length is set to be $4W$. We applied a periodic boundary condition in $x$ direction and a no-slip boundary condition is implemented in $y$ and $z$ directions. In this problem, $W$ and $U_0$ (the undisturbed centerline velocity of the channel in the absence of capsules) are used as the characteristic length and velocity scales, respectively. Here, in this work, dimensionless variables are defined as $t^* = \frac{tU_0}{W}$ (time), $\mathbf{x}^* = \frac{\mathbf{x}}{W}$ (position), $\mathbf{u}^* = \frac{\mathbf{u}}{U_0}$ (velocity), and $P^* = \frac{pW}{\mu U_0}$ (pressure). Hence, the dimensionless numbers governing the problem are: (1) the Reynolds number $Re = \frac{\rho U_0 2W}{\mu}$ that rep-

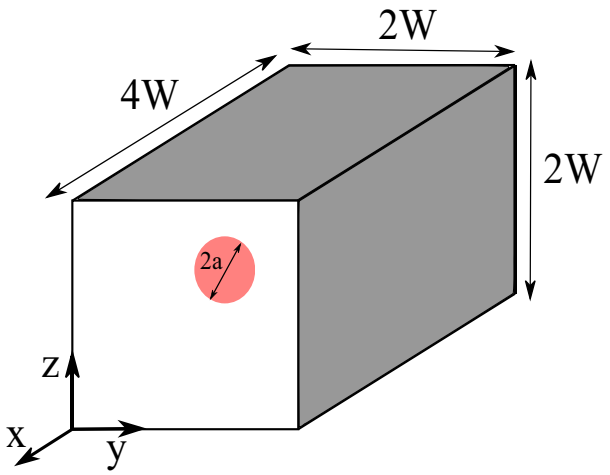


**Fig. 1** Schematic of problem setup

resents the ratio of inertial to the viscous forces; (2) the Laplace number $La = \frac{2\rho E_s a}{\mu^2}$ denoting the deformability of the cell; (3) $\phi$ that shows the volume fraction of cells in the microchannel; (4) the Weissenberg number $Wi = \frac{\lambda U_0}{W}$ showing the ratio of elastic to viscous forces; (5) $\beta = \frac{\mu_p}{\mu}$ representing the ratio of the polymer viscosity to total viscosity ($\mu = \mu_s + \mu_p$); and finally (6) the aspect ratio $AR = \frac{a}{W}$ that shows the blockage ratio in the microchannel. We assume that the inner fluid of the cells is a Newtonian fluid with a density and viscosity equal to those of the outer fluid ($(\mu_s + \mu_p)_{outer} = (\mu_s)_{inner}$ and $\rho_{inner} = \rho_{outer}$). Unless otherwise stated, $\beta$ is set to 0.9 and the cells are initially spherical. The computational domain and cell membrane are discretized using $128 \times 76 \times 76$ Eulerian grid points in $x$, $y$, and $z$ directions and 20,000 Lagrangian grid points. The mesh and domain size independency tests are provided in the "Appendix".

## 3 Results and discussion

### 3.1 Newtonian fluid

In this section, the migration of cells flowing in a Newtonian fluid is investigated and the effects of various factors including deformability ($La$), cell volume fraction ($\phi$), inertia ($Re$), and cell size ($\frac{a}{W}$) on the cell distribution are explored. The computational domain is filled with a homogeneous suspension of randomly distributed cells (cells with the same size and deformability) along the channel. A constant pressure gradient is applied to generate a flow in the microchannel and cells flow and migrate across the microchannel due to cell–cell and cell–fluid interactions. The simulation is run long enough that the suspension reach a statistically steady state. The Reynolds number is set to 37.8 unless otherwise stated.

Figure 2 illustrates the cell suspension at two time instances $t^* = 0$ and $t^* = 1336$ for $La = 1$, $\phi = 10\%$ and $\frac{a}{W} = 0.2$. The cells interact and deform in the channel. Due to the low shear rate in the central region of the channel, cells maintain their initial spherical shape, while cell deformation is more significant as the cells get closer to the wall, where the shear rate is higher. Cells migrate in the cross-stream direction and accumulate near the center of the channel. This migration behavior toward the centerline is caused by the deformability-induced force acting on the cells. The interplay between this force, inertial lift force, and wall-induced force determines the focal location of cells (Raffiee et al. 2017b; Schaaf and Stark 2017; Kilimnik et al. 2011) in the microchannel. In addition to the above-mentioned forces, the cell–cell interaction becomes important when we consider cell suspensions at a moderate volume fraction. The

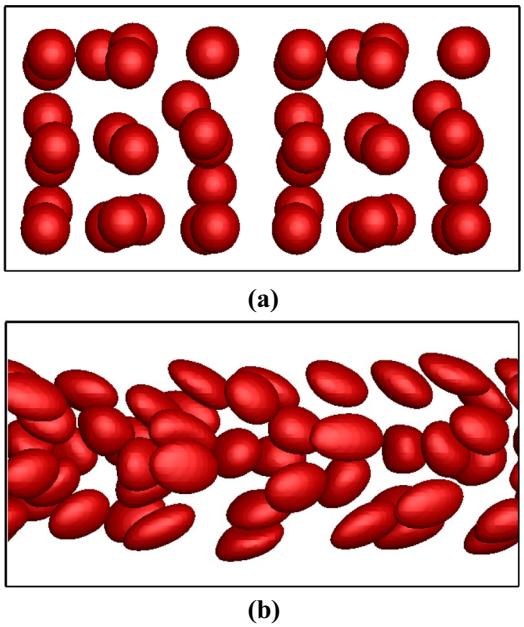


**Fig. 2** Distribution of cells at **a** $t^* = 0$ and **b** at $t^* = 1336$ for $\phi = 10\%$, $\frac{a}{W} = 0.2$, $La = 1$ and $Re = 37.8$

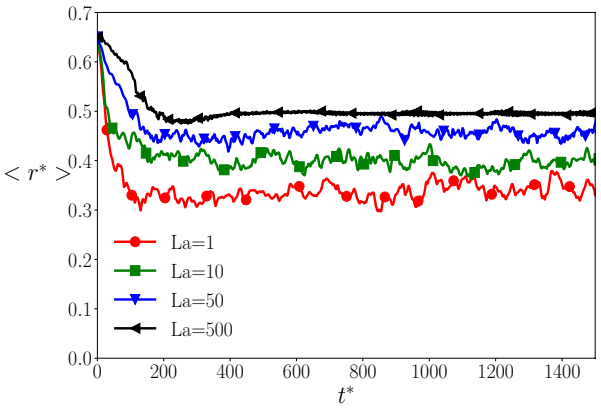


**Fig. 3** Average cell distance from the centerline for $\phi = 10\%$, $\frac{a}{W} = 0.3$ and $Re = 37.8$

migration of cells toward the center can also be observed by comparing cell distribution at two different time instances, as shown in Fig. 2, where the accumulation of cells near the center of channel is significant. To study the motion of a suspension of cells, the ensemble average of cell distance from the centerline $\langle r^* \rangle$ is computed. Figure 3 shows the temporal evolution of average distance of cells from the channel centerline for various $La$ numbers at $\phi = 10\%$, $\frac{a}{W} = 0.3$. According to this figure, $\langle r^* \rangle$ initially decreases and reaches a quasi-steady state. The initial decrease in $\langle r^* \rangle$ shows the net migration of cells toward the centerline due to the deformability-induced force acting on the cells. The steady value of cell position is computed by temporally averaging $\langle r^* \rangle$

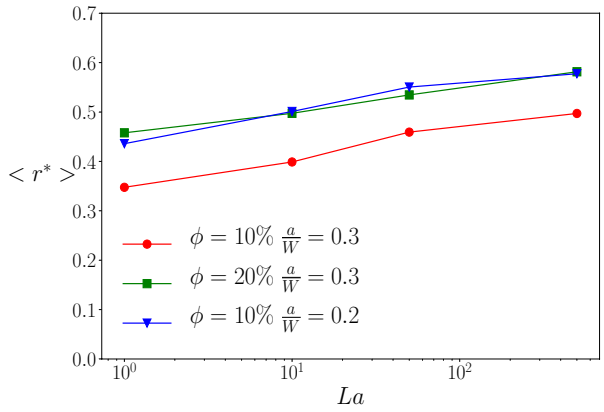


**Fig. 4** Time-averaged cell distance from the centerline for various $La$ at $Re = 37.8$

over the time period during which statistically steady state is reached (see Fig. 4 for $Re = 37.8$). The cell distance from centerline increases with increasing $La$ number (decreasing deformability) which is in agreement with the behavior of a single cell in a microchannel (Raffiee et al. 2017b; Schaaf and Stark 2017; Kilimnik et al. 2011). This change is attributed to the effect of $La$ number on the deformability-induced force. As $La$ increases, this force gets weaker and the inertial and wall-induced forces become dominant factors. Hence, the location of cells with a high Laplace number is close to that of solid particle flowing in a microchannel. Figure 4 also exhibits that increasing the cell volume fraction leads to increase in the cell distance from the channel centerline. This behavior is due to the increase in the cell–cell interaction as the number of cells flowing in the channel increases. Furthermore, the cell size has an important role on the net motion of cells. Comparing the average distance for different blockage ratios ($\frac{a}{W} = 0.2$ and 0.3) indicates that bigger cells get closer to the centerline. According to Schaaf et al. Schaaf and Stark (2017), the deformability-induced forces scale proportionally with the size of the cells. Hence, bigger cells experience a larger force towards the centerline. To study the quasi-steady distribution of cells in a microchannel, two quantities including radial volume fraction ($\phi_r$) and local volume fraction ($\phi_l$) are defined. The local volume fraction represents the cell distribution across the microchannel and is defined as the fraction of volume $\Delta y \Delta z L_x$ ($L_x$ is the channel length in x direction) occupied by the cells at different $y$ and $z$ across the channel cross section. To find $\phi_r$, Eq. (11) is introduced:

$$\phi_r = \frac{1}{A_{r,r+\Delta r}} \int_r^{r+\Delta r} \phi_l 2\pi r dr, \tag{11}$$

In this equation, $r$ is the distance from the channel centerline and $A_{r,r+\Delta r}$ is the area between $r$ and $r + \Delta r$. Hence, the radial volume fraction ($\phi_r$) is the fraction of microchannel volume between $r$ and $r + \Delta r$ that is occupied by cells. The radial volume fraction for $\phi = 10\%$, $\frac{a}{W} = 0.3$ is plotted for various Laplace number in Fig. 5a. According to this figure, the cells are not evenly distributed across the channel. The results show that the radial volume fraction of cells decreases with the distance from the channel centerline and it reaches to zero at a particular radius. The region in the microchannel in which the radial volume fraction is zero is called cell-free layer (CFL). The formation of this layer has been numerically and experimentally observed in the previous studies (Pranay et al. 2012; Zhao et al. 2012). Furthermore, the same phenomenon occurs in blood vessels, where the concentration of the red blood cells close to the vessel wall is far less than its value in the core region (Fedosov et al. 2010). The thickness of this layer is an important factor in designing microfluidic devices as it specifies the gap between the wall and suspending cells in the sample, where the rare cells should move to easier get separated. One of the important factors affecting the thickness of CFL

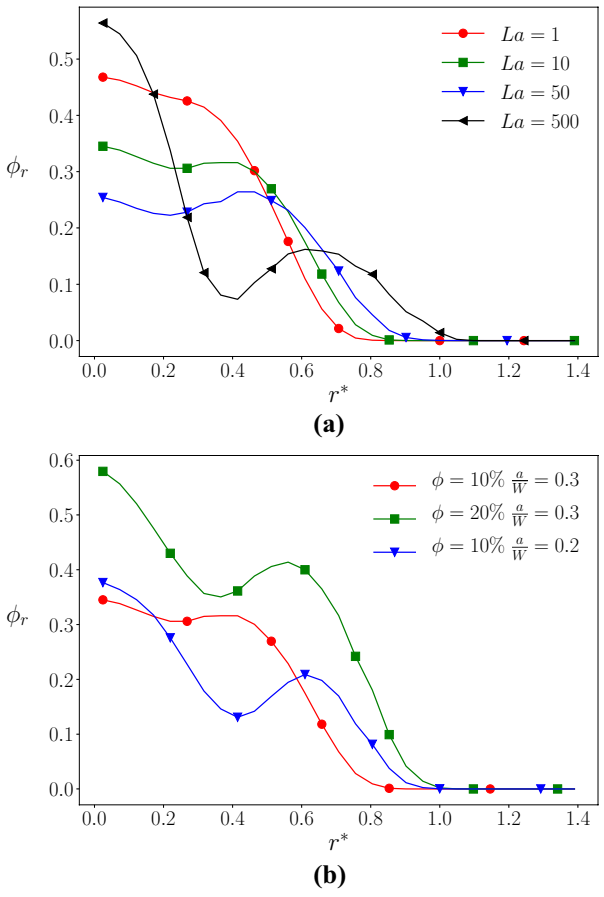


**Fig. 5** Radial volume fraction for **a** $\phi = 10\%$, $\frac{a}{W} = 0.3$ and $Re = 37.8$ and **b** for $La = 500$ and $Re = 37.8$

is *La* number. The thickness of CFL increases with decreasing *La* number (Fig. 5a). The reason for this behavior is the tendency of deformable cells to migrate toward the core region and this tendency is enhanced by decreasing *La* number. Hence, the concentration of cells is higher in the central region leading to a thicker cell-depleted layer near the wall. The maximum radial volume fraction of cells at $La = 1$ occurs at the centerline and it decreases monotonously with the distance. The occurrence of the peak at the centerline is caused by two factors: (1) cell migration toward the centerline that yields to a significant cell accumulation in that region and (2) the small area of the region ($A_{r,r+\Delta r}$) over which the radial volume fraction is computed in the central region. As the Laplace number increases, an off-center peak in the radial volume fraction occurs, although the maximum radial volume fraction still occurs at the centerline due to the aforementioned reasons. To better understand this trend in cell distribution, the effect of deformability on the focal position of cells should be considered. Increasing the *La* number pushes the focal position of cells toward the wall of a microchannel (Raffiee et al. 2017b; Schaaf and Stark 2017). Therefore, a significant increase in the local volume fraction of cells is observed at off-center locations in the cross section. This rise in the local volume fraction leads to the second peak in the radial volume fraction in Fig. 5a. The effect of the cell volume fraction ($\phi$) and the cell size on the cell distribution is plotted in Fig. 5b. The thickness of CFL decreases with $\phi$ due to the increase in the number of cells and their interaction. Hence, the cells are more spread across the channel cross section leading to a decrease in CFL thickness. Furthermore, decrease in the cell size results in decrease in the CFL thickness. This effect is attributed to the role of the cell size on the equilibrium position of cells, as shown in Fig. 4. The formation of the second peak is also observed for all the cases, as shown in Fig. 5b. To elaborate the formation of the second peak in the radial volume fraction in details, the local volume fraction of cells ($\phi_l$) in the channel cross section at $\phi = 20\%$, $La = 10$, and $\frac{a}{W} = 0.3$ is plotted in Fig. 6. The blue region near the channel wall with zero concentration of cells is the cell-free layer. According to this figure, $\phi_l$ has its maximum values at the center and at off-center locations shown by red regions. The off-center red regions in the channel cross section lead to the formation of the second peak in radial volume fraction ($\phi_r$) in Fig. 5. This phenomenon is also observed in the previous studies (Pranay et al. 2012; Li and Pozrikidis 2000) in which suspension of droplets and capsules was studied.

One of the important factors in evaluating the performance of microfluidic devices is the sample throughput. Hence, we plot the dimensionless volumetric flow rate of the suspension exiting the microchannel ($Q^*$) for various Laplace numbers, as shown in Fig. 7. Our results show that the volumetric flow rate decreases with increasing Laplace

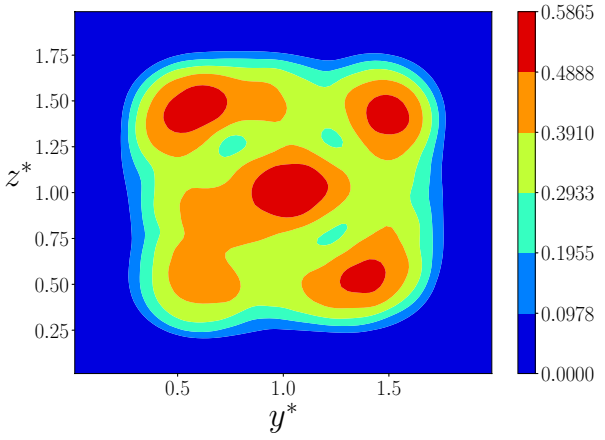


**Fig. 6** Local volume fraction of cells at $\phi = 20\%$, $La = 10$, $\frac{a}{W} = 0.3$, and $Re = 37.8$

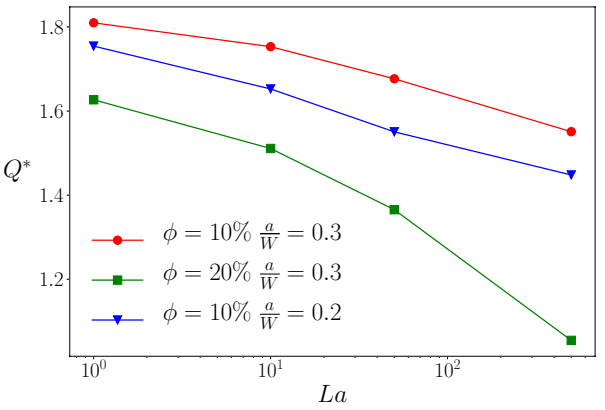


**Fig. 7** Volumetric flow rate of the suspension for various *La*, $\phi$, and size at $Re = 37.8$

number. This effect can be elaborated by considering the single-cell dynamics in a microchannel. According to our previous study (Raffiee et al. 2017b), a single-cell flowing in the microchannel lags the surrounding fluid and its velocity is smaller than the local velocity of the fluid in the absence of the cell. This effect becomes more significant, as the Laplace increases. Hence, the reduction of volumetric flow rate with increase in *La* is expected. To quantify the effect of the cell deformability on the flow field, the velocity profile in the cross section of microchannel is plotted for various *La* in Fig. 8. Our results show that decreasing the cell deformability results in decrease in the velocity across the cross section. Furthermore, the velocity profiles for various *La* numbers are identical in the cell-depleted region, while they are different in the regions occupied by the flowing cells. Figure 7 shows that the volumetric flow rate is also influenced by the cell volume fraction ($\phi$) and the cell size. Accordingly, the reduction in the volumetric flow rate

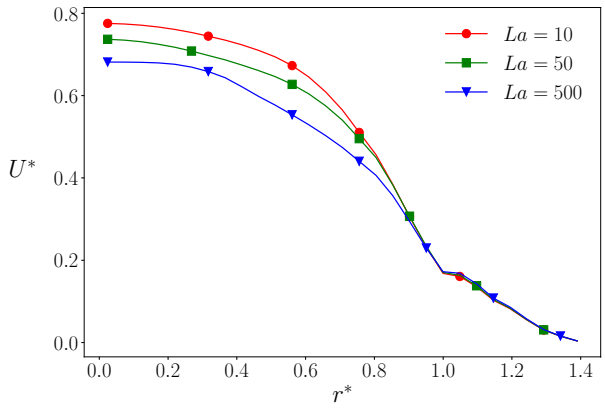


**Fig. 8** Velocity profile in the microchannel at $\phi = 10\%$, $\frac{a}{W} = 0.3$, and $Re = 37.8$

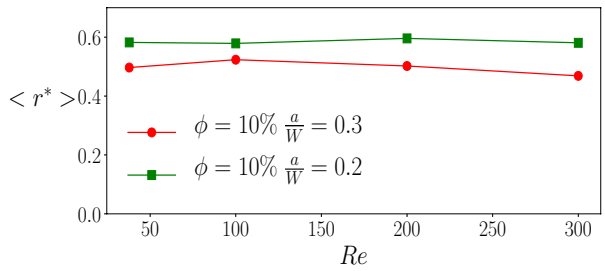


**Fig. 9** Average cell distance for $\phi = 10\%$, $La = 500$, and $\frac{a}{W} = 0.2$ and 0.3

is observed with increasing the volume fraction ($\phi$), while increasing the cell size ($\frac{a}{W}$) enhances $Q^*$. Here, we also study the effect of Reynolds number on the cell migration in the microchannel. In this work, we simulate the motion of cells at $\phi = 10\%$, $La = 500$ and two different cell sizes ($\frac{a}{W} = 0.2$ and 0.3) for various $Re$ numbers. The average distance of the cells ($\langle r^* \rangle$) is plotted in Fig. 9. Our result shows that the average cell distance is not influenced by Reynolds number. This behavior is in agreement with previous studies (Li et al. 2015; Raffiee et al. 2017b) that investigated the dynamics of a solid particle and a deformable capsule with high $La$ number in a microchannel. Furthermore, the radial volume fraction distribution ($\phi_r$) for the cell suspension with $\frac{a}{W} = 0.2$ is plotted in Fig. 10. This result also emphasizes that the steady spatial distribution of flowing cells is not affected by the Reynolds number and the change in the CFL thickness is negligible.

## 3.2 Viscoelastic fluid

In this section, the effect of the polymeric fluid on the cell migration behavior is investigated. As it is mentioned in Sect. 3.1, the migration of the cells is governed by the

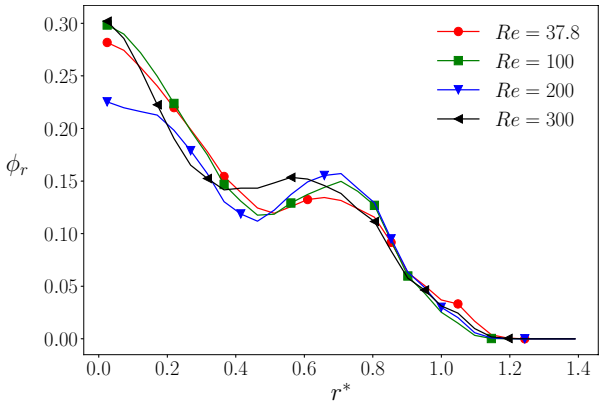


**Fig. 10** Radial volume fraction distribution for $\phi = 10\%$, $La = 500$, and $\frac{a}{W} = 0.2$

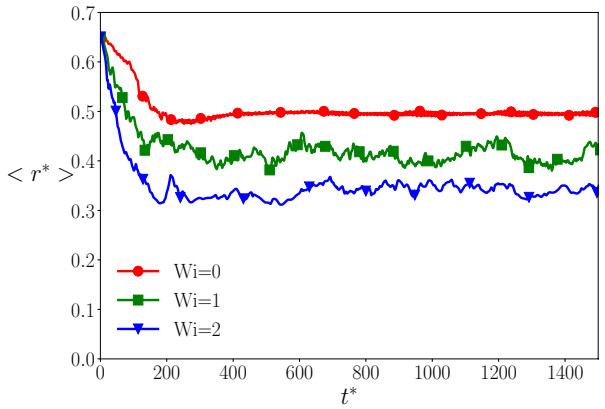


**Fig. 11** Temporal evolution of cell distance from the centerline for $\phi = 10\%$, $\frac{a}{W} = 0.3$, $La = 500$, and $Re = 37.8$

interplay between inertial lift force, deformability-induced force, wall-induced force, and cell–cell interaction. However, the cells flowing in a polymeric fluid experience an elastic force in addition to other forces. The elastic force is generated due to the deformation of polymer chains in the channel flow. The interplay between various forces determines the cell distribution in the channel. The motion and consequently the time-averaged distance of cells suspended in a polymeric fluid is significantly influenced by the fluid elasticity.

Figure 11 plots the temporal evolution of the average cell distance from the channel centerline at $\phi = 10\%$, $La = 500$ and $\frac{a}{W} = 0.3$ for various $Wi$ numbers ($Wi = 0$ corresponds to a Newtonian fluid). Our results show that the cell distance decreases as $Wi$ number increases. Therefore, a constant-viscosity viscoelastic fluid pushes the cells toward the channel centerline. This behavior is in agreement with the previous numerical and experimental studies (Raffiee et al. 2017b; Li et al. 2015; Lim et al. 2014) for an isolated cell. This result

suggests that the polymeric fluid can be used as a passive method in devices in which the main goal is cell focusing at the centerline such as cytometers. Furthermore, this method adds another variable to be tuned by the user to control the focal position of the cells in microfluidic devices. According to the results, the deformability-induced force and elastic force have reinforcing effect that drives the cells toward the centerline, while the inertial force has the opposite effect that pushes the cells toward the channel wall. Therefore, for a low $Wi$ number, the inertial force is dominant and the resulting average cell distance is close to that of cells flowing in a Newtonian fluid, while for a high $Wi$ number, the elastic force has a significant effect and the cells accumulate near the centerline. To observe the effect of the polymeric fluid, the cell-fraction distribution of the cells with $\frac{a}{W} = 0.2$, $La = 500$ and $\phi = 10\%$ is plotted in Fig. 12. This figure shows the extent to which the cells are distributed across the microchannel. The fraction of cells located close to the centerline increases and the fraction of the cells close to the wall decreases significantly with increasing the $Wi$ number. The cell fraction at $r^* = 1.38$ and 1.12 reaches nearly to zero. Furthermore, the location at which the maximum cell fraction occurs approaches to the centerline when polymers are added to the flowing fluid. The polymeric effect is also exhibited in Fig. 13, which shows the cell configuration for $\phi = 10\%$, $La = 500$ and $\frac{a}{W} = 0.2$ for two different values of Weissenberg number ($Wi = 0$ and 2). According to this figure, the cells flowing in a constant-viscosity viscoelastic fluid (Fig. 13b) focus more near the centerline compared to the cells flowing in a Newtonian fluid (Fig. 13a). To quantify the effect of polymeric fluid, the time-averaged cell distance for various cell sizes and volume fractions is plotted as a function of $Wi$ number in Fig. 14. The cell distance from the centerline decreases with increase in $Wi$ number for various $\phi$ and $\frac{a}{W}$. The decrease in time-averaged cell distance continues until the $Wi$ number reaches a critical value above

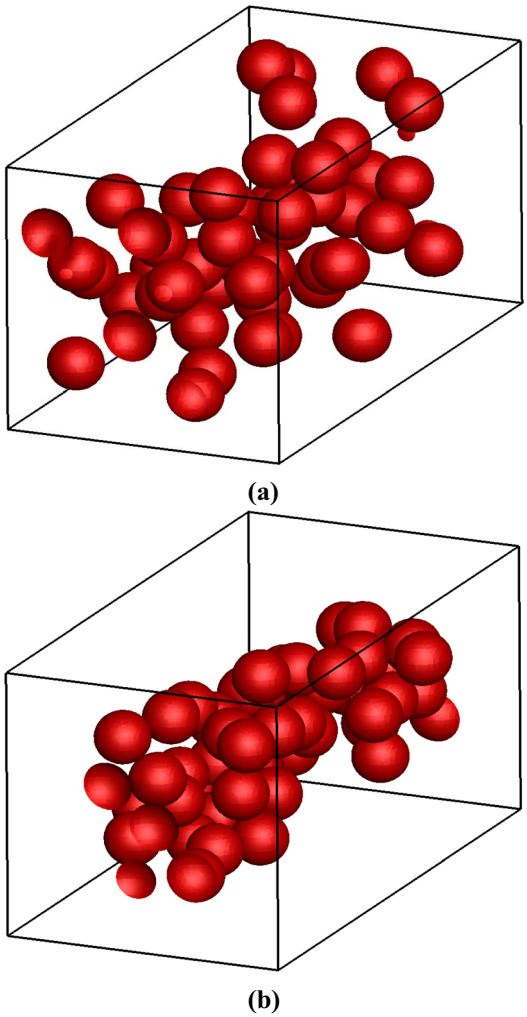


**Fig. 13** Distribution of cells at $\phi = 10\%$, $La = 500$, $Re = 37.8$, $\frac{a}{W} = 0.2$ and **a** $Wi = 0$ and **b** $Wi = 2$

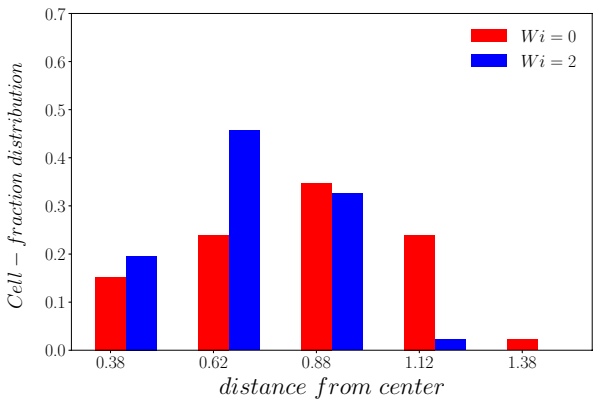


**Fig. 12** Cell-fraction distribution of cells with $\frac{a}{W} = 0.2$, $La = 500$, and $\phi = 10\%$ with $Wi = 0$ and 2

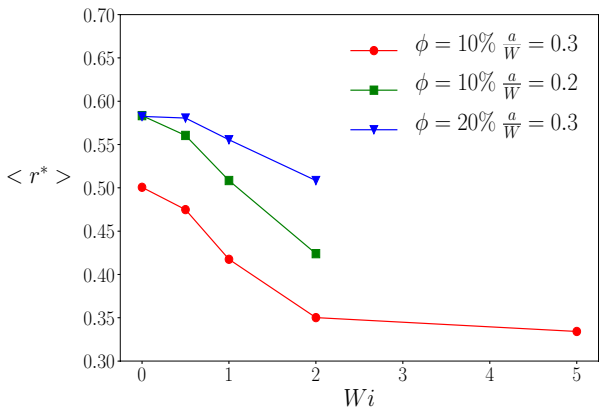


**Fig. 14** Time-averaged cell distance from the centerline for various $Wi$ numbers at $Re = 37.8$

which the cell distance does not reduce further and reaches a plateau. This behavior is attributed to the cell–cell interaction that has an opposing effect against elastic effect and does not allow the cells to focus at the centerline. In other words, the cells are accumulated in the core region and the distance between the cells cannot be further reduced. This effect can be seen in Fig. 13b that illustrates the distribution of cells in the central region. As it is shown in Fig. 14, the cell distance is not computed for $Wi$ above 2 for two cases ($\phi = 20\%$, $\frac{a}{W} = 0.3$ and $\phi = 10\%$, $\frac{a}{W} = 0.2$). The lack of data for these cases is due to the numerical instability occurring for larger $Wi$ numbers and volume fractions. The effect of the cell volume fraction ($\phi$) and the cell size ($\frac{a}{W}$) is similar to their effect in a Newtonian fluid. Increasing the volume fraction increases the cell distance and increasing the cell size decreases the cell distance from the centerline. To study the effect of elasticity on CFL thickness, the radial volume fraction is plotted in Fig. 15 for $\phi = 10\%$, $\frac{a}{W} = 0.3$, and $Re = 37.8$. The thickness of the CFL increases with increasing $Wi$ number. This change is attributed to the polymer chains driving the cells more effectively toward the centerline with increasing $Wi$ number. Hence, a larger region in the vicinity of channel walls remain depleted from the cells. Furthermore, the location of the off-center peak in the radial volume fraction of the cells approaches to the centerline as the elasticity of the suspending fluid increases which is also due to the enhanced tendency of the cells in accumulating in the core region. The effect of the polymeric fluid on the throughput of microfluidic devices is also studied in this section. The volumetric flow rate of the exiting suspension is measured under various $Wi$ numbers and constant pressure gradient at $\phi = 10\%$, $\frac{a}{W} = 0.3$, and $Re = 37.8$ and is plotted in Fig. 16a. Our results show that the volumetric flow rate increases with increasing $Wi$ number. To elaborate this effect, the velocity profile of the corresponding cases in the channel cross section is plotted in Fig. 16b. As $Wi$ number

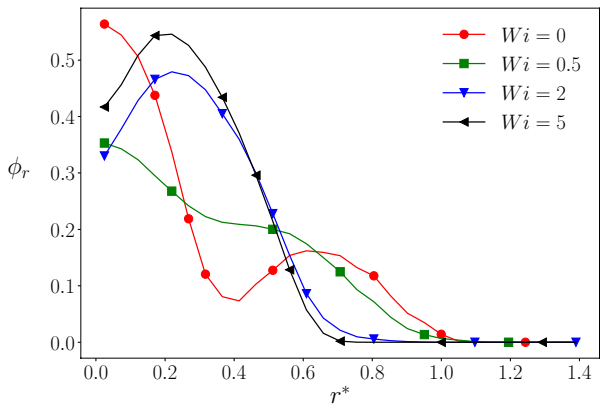


**Fig. 15** Radial volume fraction of cells for $\phi = 10\%$, $\frac{a}{W} = 0.3$ and $Re = 37.8$

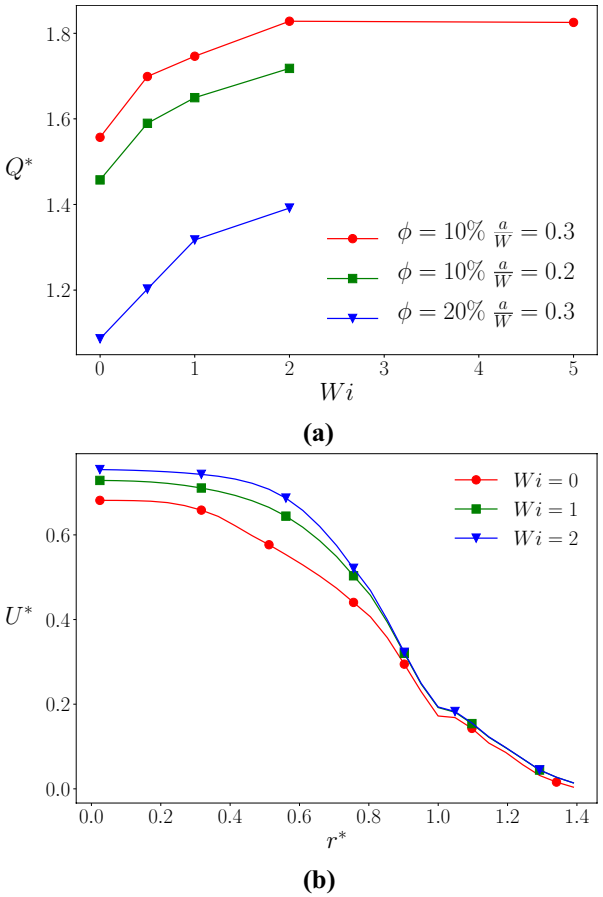


**Fig. 16** **a** Volumetric flow rate of suspension for various $Wi$ numbers at $Re = 37.8$ and **b** the velocity profile at $\phi = 10\%$, $La = 500$, $\frac{a}{W} = 0.3$ and $Re = 37.8$

increases, the velocity at centerline ($r^* = 0$) increases and the velocity profile becomes flatter in the central region. Therefore, the change in the velocity distribution across the microchannel due to the change in fluid elasticity results in the enhanced sample throughput in microfluidic devices. Furthermore, Fig. 16a shows that there is a critical $Wi_c$ number above which the volumetric flow rate reaches a plateau. This change is attributed to the accumulation of cells in the core region, where cells cannot be more compact above the critical $Wi_c$ number. Besides, the effect of Reynolds number on the performance of the microfluidic devices in presence of polymeric fluids is investigated. The time-averaged cell distance is plotted for various $Re$ numbers at $\phi = 10\%$, $La = 500$ and $Wi = 2$ in Fig. 17. As it is shown, the distance of the cells from the centerline increases with increasing the $Re$ number. This finding is in agreement with the previous studies (Raffiee et al. 2017b; Li et al. 2015) in which the dynamics of an isolated solid and deformable particle were studied in a microchannel. This behavior can be elaborated according to the strong dependence of inertial and elastic forces on $Re$ number. The interaction between various forces

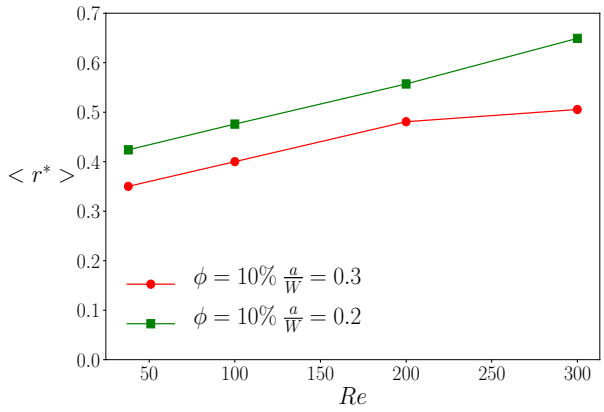


**Fig. 17** Time-averaged cell distance for various $Re$ numbers at $\phi = 10\%$, $La = 500$ and $Wi = 2$

such as inertial and elastic forces determines the final position of cells in the microchannel. The inertial effect is the dominant factor when $Re \gg Wi$ and the cells are expected to be driven toward the walls, while for the case with $Wi \gg Re$, the elastic force becomes dominant and the cells tend to accumulate in the central region of the microchannel.

## 4 Conclusions

In this work, the dynamics of a cell suspension flowing in Newtonian and viscoelastic fluids is investigated. We study the effect of the cell size ($\frac{a}{W}$), cell volume fraction ($\phi$), inertia ($Re$), deformability ($La$), and fluid elasticity ($Wi$) on the motion of cell suspension and the performance of the microfluidic devices composed of a straight microchannel. The variation of the aforementioned factors modulates the governing forces and influences the distribution of cells in the microchannel. Our results show that increasing the $La$ number leads to the increase in the cell distance from the channel centerline ($r^*$) and reduction in the volumetric flow rate of the exiting flow ($Q^*$). These variables are also affected by the cell size and cell volume fraction. Decreasing the cell size pushes the cells further toward the wall and this effect can be reinforced by increasing the cell volume fraction. However, the increase in $\frac{a}{W}$ and $\phi$ has an opposite effect on the volumetric flow rate and causes the decrease in $Q^*$. Our findings suggest that adding a polymer in suspending fluid pushes the cells further toward the centerline compared to a Newtonian fluid and can be used in devices that require centerline focusing of the cells such as cytometers. It is shown that increasing fluid elasticity ($Wi$) yields the reduction in cell distance from the centerline, while it increases the volumetric flow rate of the exiting flow. Furthermore, the effect of the inertia ($Re$) is investigated for both Newtonian and viscoelastic fluids. The results indicate that the change in the Reynolds number does not significantly affect the suspension dynamics, while an opposite behavior is observed in a viscoelastic fluid in which the cells are driven further toward the wall due to increase in the inertial effects.

**Acknowledgements** This research was partially supported by a Grant from National Science Foundation [CBET-1705371].

## Compliance with ethical standards

**Conflict of interest** There are no conflicts of interest to declare.

## Appendix

To check the mesh and the domain size independency of the computational results, we follow the method used in Doddi and Bagchi (2009), where the volumetric flow rate of the flow is investigated for various grid and domain sizes. Figure 18a shows the volumetric flow rate of the cell suspension in a Newtonian fluid at $Re = 100$, $\phi = 10\%$ and $\frac{a}{W} = 0.3$ for various $La$ numbers with $128 \times 76 \times 76$ and $200 \times 133 \times 133$ grid points in $x$, $y$, and $z$ directions, respectively. The maximum error between two different grid sizes is 2.44%. Hence, our results indicate that the numerical simulation performed in this study is independent of the mesh sizes. The results for the domain independency of the simulation are also plotted in Fig. 18b. The variation of the volumetric flow rate at $Re = 100$, $\phi = 10\%$, and $\frac{a}{W} = 0.3$ for two different domain sizes ($L_x = 4W$ and $8W$) in the $x$ direction along which the

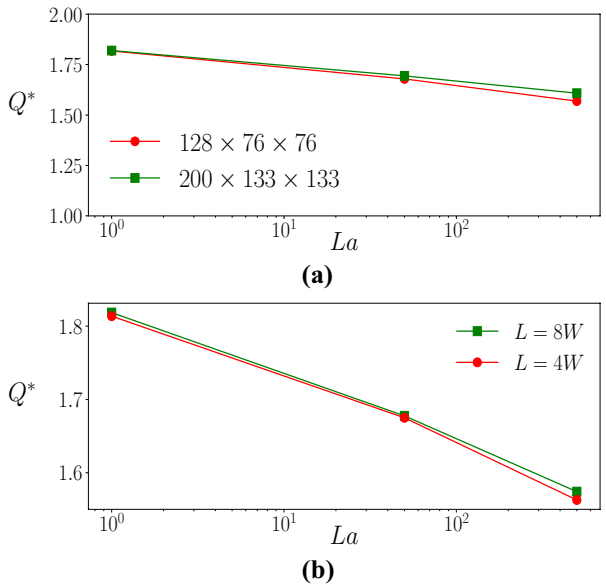


**Fig. 18** Volumetric flow rate at $Re = 100$, $\phi = 10\%$ and $\frac{a}{W} = 0.3$ **a** for $128 \times 76 \times 76$ and $200 \times 133 \times 133$ grid points and **b** for $L_x = 4W$ and $8W$ in $x$ direction

periodic boundary condition is considered. The maximum error between two channel geometries is 0.71% that proves the independency of the numerical results against the computational domain size.

## References


Asmolov ES (1999) The inertial lift on a spherical particle in a plane poiseuille flow at large channel Reynolds number. J Fluid Mech 381:63–87

Chang K-S, Olbricht WL (1993) Experimental studies of the deformation and breakup of a synthetic capsule in steady and unsteady simple shear flow. J Fluid Mech 250:609–633

Charrier J, Shrivastava S, Wu R (1989) Free and constrained inflation of elastic membranes in relation to thermoforming non-axisymmetric problems. J Strain Anal Eng Des 24(2):55–74

Choi Y-S, Seo K-W, Lee S-J (2011) Lateral and cross-lateral focusing of spherical particles in a square microchannel. Lab Chip 11(3):460–465

Chorin AJ (1968) Numerical solution of the Navier–Stokes equations. Math Comput 22(104):745–762

Chung TD, Kim HC (2007) Recent advances in miniaturized microfluidic flow cytometry for clinical use. Electrophoresis 28(24):4511–4520

Cooley M, Sarode A, Hoore M, Fedosov DA, Mitragotri S, Gupta AS (2018) Influence of particle size and shape on their margination and wall-adhesion: implications in drug delivery vehicle design across nano-to-micro scale. Nanoscale 10(32):15350–15364

D'Avino G, Romeo G, Villone MM, Greco F, Netti PA, Maffettone PL (2012) Single line particle focusing induced by viscoelasticity of the suspending liquid: theory, experiments and simulations to design a micropipe flow-focuser. Lab Chip 12(9):1638–1645

D'Avino G, Greco F, Maffettone PL (2017) Particle migration due to viscoelasticity of the suspending liquid and its relevance in microfluidic devices. Annu Rev Fluid Mech 49:341–360

Del Giudice F, DAvino G, Greco F, Netti PA, Maffettone PL (2015) Effect of fluid rheology on particle migration in a square-shaped microchannel. Microfluid Nanofluid 19(1):95–104

Del Giudice F, Sathish S, DAvino G, Shen AQ (2017) From the edge to the center: viscoelastic migration of particles and cells in a strongly shear-thinning liquid flowing in a microchannel. Anal Chemi

Di Carlo D (2009) Inertial microfluidics. Lab Chip 9(21):3038–3046

Di Carlo D, Irimia D, Tompkins RG, Toner M (2007) Continuous inertial focusing, ordering, and separation of particles in microchannels. Proc Natl Acad Sci 104(48):18892–18897

Di Carlo D, Edd JF, Humphry KJ, Stone HA, Toner M (2009) Particle segregation and dynamics in confined flows. Phys Rev Lett 102(9):094503

Doddi SK, Bagchi P (2009) Three-dimensional computational modeling of multiple deformable cells flowing in microvessels. Phys Rev E 79(4):046318

Faridi MA, Ramachandraiah H, Banerjee I, Ardabili S, Zelenin S, Russom A (2017) Elasto-inertial microfluidics for bacteria separation from whole blood for sepsis diagnostics. J Nanobiotechnol 15(1):3

Fedosov DA, Caswell B, Popel AS, Karniadakis GE (2010) Blood flow and cell-free layer in microvessels. Microcirculation 17(8):615–628

Feng J, Hu HH, Joseph DD (1994) Direct simulation of initial value problems for the motion of solid bodies in a newtonian fluid part 1. Sedimentation. J Fluid Mech 261:95–134

Friend J, Yeo LY (2011) Microscale acoustofluidics: microfluidics driven via acoustics and ultrasonics. Rev Mod Phys 83(2):647

Godin J, Chen C-H, Cho SH, Qiao W, Tsai F, Lo Y-H (2008) Microfluidics and photonics for bio-system-on-a-chip: a review of advancements in technology towards a microfluidic flow cytometry chip. J Biophoton 1(5):355–376

Gossett DR, Weaver WM, Mach AJ, Hur SC, Tse HTK, Lee W, Amini H, Di Carlo D (2010) Label-free cell separation and sorting in microfluidic systems. Anal Bioanal Chem 397(8):3249–3267

Ho B, Leal L (1974) Inertial migration of rigid spheres in two-dimensional unidirectional flows. J Fluid Mech 65(2):365–400

Howell PB Jr, Golden JP, Hilliard LR, Erickson JS, Mott DR, Ligler FS (2008) Two simple and rugged designs for creating microfluidic sheath flow. Lab Chip 8(7):1097–1103

Hur SC, Tse HTK, Di Carlo D (2010) Sheathless inertial cell ordering for extreme throughput flow cytometry. Lab Chip 10(3):274–280

Karimi A, Yazdi S, Ardekani AM (2013) Hydrodynamic mechanisms of cell and particle trapping in microfluidics. Biomicrofluidics 7(2):021501

Karnis A, Goldsmith H, Mason S (1966) The flow of suspensions through tubes: V. inertial effects. Can J Chem Eng 44(4):181–193

Kilimnik A, Mao W, Alexeev A (2011) Inertial migration of deformable capsules in channel flow. Phys Fluids 23(12):123302

Krüger T, Kaoui B, Harting J (2014) Interplay of inertia and deformability on rheological properties of a suspension of capsules. J Fluid Mech 751:725–745

Kunze A, Che J, Karimi A, Di Carlo D (2015) Research highlights: cell separation at the bench and beyond. Lab Chip 15(3):605–609

Lancaster C, Kokoris M, Nabavi M, Clemmens J, Maloney P, Capadanno J, Gerdes J, Battrell C (2005) Rare cancer cell analyzer for whole blood applications: microcytometer cell counting and sorting subcircuits. Methods 37(1):120–127

Lee DJ, Brenner H, Youn JR, Song YS (2013) Multiplex particle focusing via hydrodynamic force in viscoelastic fluids. Sci Repo:3

Leonard BP (1979) A stable and accurate convective modelling procedure based on quadratic upstream interpolation. Comput Methods Appl Mech Eng 19(1):59–98

Leshansky A, Bransky A, Korin N, Dinnar U (2007) Tunable nonlinear viscoelastic focusing in a microfluidic device. Phys Rev Lett 98(23):234501

Li X, Pozrikidis C (2000) Wall-bounded shear flow and channel flow of suspensions of liquid drops. Int J Multiphase Flow 26(8):1247–1279

Li G, McKinley GH, Ardekani AM (2015) Dynamics of particle migration in channel flow of viscoelastic fluids. J Fluid Mech 785:486–505

Lim EJ, Ober TJ, Edd JF, Desai SP, Neal D, Bong KW, Doyle PS, McKinley GH, Toner M (2014) Inertio-elastic focusing of bioparticles in microchannels at high throughput. Nat Commun 2014:5

Liu C, Xue C, Chen X, Shan L, Tian Y, Hu G (2015) Size-based separation of particles and cells utilizing viscoelastic effects in straight microchannels. Anal Chem 87(12):6041–6048

Lu X, Liu C, Hu G, Xuan X (2017) Particle manipulations in non-Newtonian microfluidics: a review. J Colloid Interface Sci 500:182

Nam J, Tan JKS, Khoo BL, Namgung B, Leo HL, Lim CT, Kim S (2015) Hybrid capillary-inserted microfluidic device for sheathless particle focusing and separation in viscoelastic flow. Biomicrofluidics 9(6):064117

Paiè P, Bragheri F, Di Carlo D, Osellame R (2017) Particle focusing by 3D inertial microfluidics. Microsyst Nanoeng 3:17027

Pamme N (2006) Magnetism and microfluidics. Lab Chip 6(1):24–38

Pethig R (2010) Dielectrophoresis: status of the theory, technology, and applications. Biomicrofluidics 4(2):022811

Popel AS, Johnson PC (2005) Microcirculation and hemorheology. Annu Rev Fluid Mech 37:43–69

Pozrikidis C (2003) Modeling and simulation of capsules and biological cells. CRC Press, Boca Raton

Pranay P, Henríquez-Rivera RG, Graham MD (2012) Depletion layer formation in suspensions of elastic capsules in newtonian and viscoelastic fluids. Phys Fluids 24(6):061902

Raffiee AH, Dabiri S, Ardekani AM (2017a) Deformation and buckling of microcapsules in a viscoelastic matrix. Phys Rev E 96(3):032603

Raffiee AH, Dabiri S, Ardekani AM (2017b) Elasto-inertial migration of deformable capsules in a microchannel. Biomicrofluidics 11(6):064113

Ramanujan S, Pozrikidis C (1998) Deformation of liquid capsules enclosed by elastic membranes in simple shear flow: large deformations and the effect of fluid viscosities. J Fluid Mech 361:117–143

Romeo G, D'Avino G, Greco F, Netti PA, Maffettone PL (2013) Viscoelastic flow-focusing in microchannels: scaling properties of the particle radial distributions. Lab Chip 13(14):2802–2807

Saadat A, Guido CJ, Iaccarino G, Shaqfeh ESG (2018) Immersed-finite-element method for deformable particle suspensions in viscous and viscoelastic media. Phys Rev E 98(6):063316

Schaaf C, Stark H (2017) Inertial migration and axial control of deformable capsules. Soft Matter

Schonberg JA, Hinch E (1989) Inertial migration of a sphere in Poiseuille flow. J Fluid Mech 203:517–524

Segre G (1961) Radial particle displacements in poiseuille flow of suspensions. Nature 189:209–210

Seo KW, Kang YJ, Lee SJ (2014) Lateral migration and focusing of microspheres in a microchannel flow of viscoelastic fluids. Phys Fluids 26(6):063301

Sethu P, Sin A, Toner M (2006) Microfluidic diffusive filter for apheresis (leukapheresis). Lab Chip 6(1):83–89

Skalak R, Tozeren A, Zarda R, Chien S (1973) Strain energy function of red blood cell membranes. Biophys J 13(3):245–264

Sundararajan N, Pio MS, Lee LP, Berlin AA (2004) Three-dimensional hydrodynamic focusing in polydimethylsiloxane (PDMS) microchannels. J Microelectromech Syst 13(4):559–567

Unverdi SO, Tryggvason G (1992) A front-tracking method for viscous, incompressible, multi-fluid flows. J Comput Phys 100(1):25–37

van de Stolpe A, Pantel K, Sleijfer S, Terstappen LW, Den Toonder JM (2011) Circulating tumor cell isolation and diagnostics: toward routine clinical use

Villone M, DAvino G, Hulsen M, Greco F, Maffettone P (2013) Particle motion in square channel flow of a viscoelastic liquid: migration vs. secondary flows. J Non-Newtonian Fluid Mech 195:1–8

Yang S, Kim JY, Lee SJ, Lee SS, Kim JM (2011) Sheathless elasto-inertial particle focusing and continuous separation in a straight rectangular microchannel. Lab Chip 11(2):266–273

Zeng L, Balachandar S, Fischer P (2005) Wall-induced forces on a rigid sphere at finite Reynolds number. J Fluid Mech 536:1–25

Zhao H, Shaqfeh ES, Narsimhan V (2012) Shear-induced particle migration and margination in a cellular suspension. Phys Fluids 24(1):011902